

Measurement Methods for High-Frequency Characterizations of Permeability, Permittivity, and Core Loss of Mn-Zn Ferrite Cores

Marcin Kački ¹, Marek S. Rylko ², *Member, IEEE*, John G. Hayes ³, *Senior Member, IEEE*, and Charles R. Sullivan, *Fellow, IEEE*

Abstract—Manganese–zinc (Mn-Zn) ferrites are the primary choice for high-frequency and high-power magnetic components. Optimum material selection is essential for high-performance magnetic component design. However, the manufacturers' material specifications usually do not provide sufficient information to optimize the design. Complex permeability and permittivity, as well as specific power loss, are typically provided as one value, regardless of the core shape and size. Magnetic component design based on these incomplete specifications can result in a poorly optimized component. This article proposes methods to determine the properties of Mn-Zn ferrite at high frequencies, with tests up to 20 MHz. This article also presents experimental complex permeability and permittivity frequency characteristics for four ferrite materials: 3E10, 3F36, 3E65, and 3C95. The resulting fitted parameters for the equivalent-circuit model can be used in any design algorithm or simulation tool. The impacts of physical size, temperature and force on complex permeability and permittivity are also considered.

Index Terms—Dielectric losses, ferrite, magnetic losses, magnetic materials, permeability measurement, permittivity.

I. INTRODUCTION

THE continuous drive for high-performance energy conversion and the application of wide bandgap semiconductors is triggering demand for high-performance magnetic components. Due to the high-frequency capabilities, manganese–zinc (Mn-Zn) ferrites are of primary interest for the investigation of high-performance magnetic components. Higher switching frequencies set new limits to magnetic component design and magnetic material selection. Ferrite manufacturers have responded to the increased demand with improved Mn-Zn ferrites and offer

low-cost materials with lower losses and higher permeability. However, the combination of the high permeability and the high permittivity of Mn-ZN ferrite affects the high-frequency performance due to eddy currents and dimensional resonance [1]–[8]. By default, the ferrite manufacturers' specifications provide average material characteristics, which may be of limited use for detailed analysis. State-of-the-art magnetic modeling often assumes that the high-frequency effects in ferrites are negligible. The material definition follows the manufacturers' specifications with ferrite parameters provided as a constant for the entire ferrite family range. This makes the core material selection during the design somewhat cumbersome due to excessive design iterations. The poor quality of the material data jeopardizes accurate modeling; therefore, high-fidelity characteristics of magnetics materials are required. The magnetic material may be characterized by its complex permeability and permittivity. These two parameters are of differentiated physical origin, and so two independent measurements are required. Measurement fixtures on the market that determine the ferrite's complex characteristics are limited to ring cores with an external diameter between 25 and 30 mm [10], [11]. The available fixtures are effective up to 1 MHz as sample size is affected by the frequency effects; thus, a new approach to ferrite electrical properties measurements is required to determine magnetic material properties beyond 1 MHz. Core power losses for large-field amplitudes are presented in addition to the frequency complex characteristics to give a complete picture of the magnetic material characterization.

The fundamental work on novel measurement methods for high-frequency properties of magnetics materials presented in [12]–[14] was mainly focused on complex permittivity measurements.

In this article, the measurement methods are extended to the measurement of permeability and core loss. Thus, the novelty of this article is in the development of measurement methods and in the aggregation and comparison of the ferrite properties of permeability, permittivity, and power loss. Material properties for a range of low- and high-permeability ferrite cores are presented in this article for the first time.

This article introduces a method to determine the high-frequency properties of Mn-ZN ferrites by the elimination of eddy currents and dimensional-resonance effects. Thus, the obtained natural material characteristics are ready for use in any

Manuscript received 25 February 2022; revised 12 May 2022; accepted 24 June 2022. Date of publication 11 July 2022; date of current version 6 September 2022. An earlier version of this paper was presented in part at the 2020 IEEE Applied Power Electronics Conference and Exposition (APEC) [DOI: 10.1109/APEC39645.2020.9124101]. Recommended for publication by Associate Editor M. Chen. (*Corresponding author: John G. Hayes.*)

Marcin Kački and Marek S. Rylko are with the R&D, SMA Magnetics sp. z o.o., 32-085 Modlniczka, Poland (e-mail: marcin.kacki@sma-magnetics.com; marek.rylko@sma-magnetics.com).

John G. Hayes is with the Electrical Engineering, University College Cork, T12 YN60 Cork, Ireland (e-mail: john.hayes@ucc.ie).

Charles R. Sullivan is with the Thayer School of Engineering, Dartmouth College, Hanover, NH 03755 USA (e-mail: charles.r.sullivan@dartmouth.edu). Color versions of one or more figures in this article are available at <https://doi.org/10.1109/TPEL.2022.3189671>.

Digital Object Identifier 10.1109/TPEL.2022.3189671

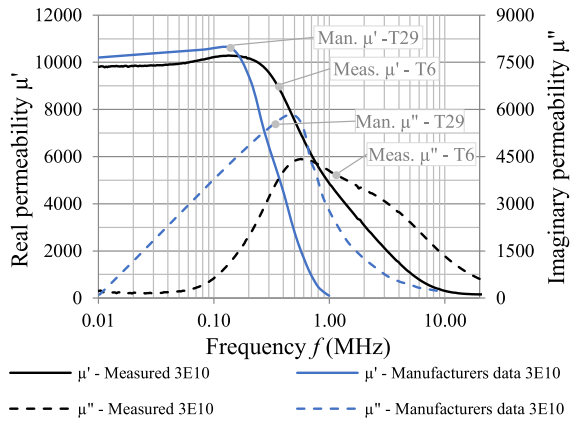


Fig. 1. Complex permeability versus frequency of 3E10 ferrite based on experimental and manufacturers data.

design models, and so, eliminate the need to measure complex characteristic for the different core sizes. The physical size of the sample impact on complex permeability measurements is characterized in Section II. A practical method to extrapolate the high-frequency complex permittivity of ferrites and related measurement results for higher frequencies is covered in Section III. Section IV describes the compression force influence on complex permeability and permittivity measurements. Core power loss analysis is shown in Section V. Finally, Section VI concludes this article. Appendix I presents experimental magnetic material permeability and permittivity characteristics for additional materials: 3E10, 3F36, 3E65, and 3C95.

II. COMPLEX PERMEABILITY

Analysis of the frequency characteristics of the complex permeability is the primary method to assess the ferrite material performance at a low-field amplitude. The complex permeability is expressed by its real (reactive) component μ' and imaginary (dissipative) component μ'' . The complex impedance \bar{Z} can be represented by the series model based on complex permeability

$$\bar{Z} = j\omega L_S + R_S = j\omega L_0 (\mu'_S - j\mu''_S) \quad (1)$$

where R_S and L_S are the series resistance and the series inductance, respectively, L_0 is the inductance of the core with unity permeability, ω is the angular frequency, j is the complex operator, and μ' and μ'' are the real and imaginary permeabilities in the series model.

Complex permeability characteristics included in the manufacturers' specifications are often measured based on a relatively small core, such as T29. Unfortunately this core is still too big to provide material characteristics without visible high-frequency effects. As an example, a comparison between the material complex permeability measured for the T29 and the T6 cores for 3E10 material is presented in Fig. 1. The results obtained for T29 core by the author correlate with the results in manufacturers' specifications [15]. As can be seen, the dimensions of the tested T29 ferrite sample (blue line) significantly affect the measured core permeability characteristics compared with the high-fidelity T6 core (black line) permeability measurements.

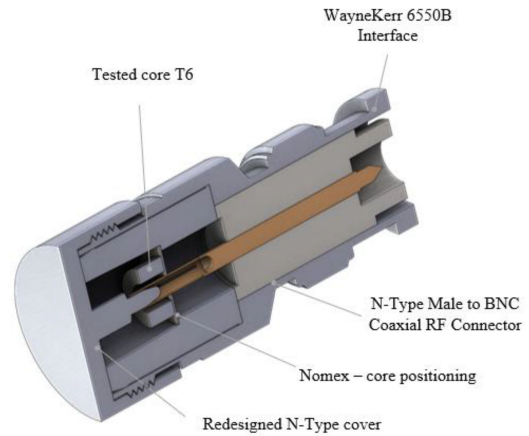


Fig. 2. Complex permeability measurement fixture for T6 cores.

The dimensions of the tested Mn-Zn ferrites may affect the measured core permeability characteristics; therefore, the selected core should have the smallest dimensions possible. On the other hand, the small core dimensions directly translate to small values of measured resistance and reactance. In order to avoid additional error, special attention should be paid to the measurement device selection. The selected frequency analyzer has a measurement error of up to 4% for the frequency range of interest. The toroidal core T6/4/2.8 mm has been selected as the core which provides the material data with the highest possible accuracy as it comes through the press and sintering process without additional machining that may affect material parameters. The test fixture developed to define the complex permeability of the T6 core is presented in Fig. 2. The test fixture may be easily duplicated as it is built with off-the-shelf parts. Therefore, the material complex permeability characteristics for the T6 core, made of various materials, can be easily reproduced.

A. Complex Permeability Physical Sample Size Effect

In this section, the determination of the complex permeability is experimentally investigated. In order to expose the core size effect, the experiment is designed to validate a number of samples of various sizes, as given in Table I.

Since the core size varies, the tests requires a customized measurement fixture. Construction of the fixture provides for a single turn equally distributed around the toroidal core specimen. The fixture in the shape of a cylindrical cup forms a short-ended coaxial line over the tested core. This measurement method provides accurate results and allows for measurements up to 1 GHz [16], [17]. Measurements are performed with a Wayne Kerr 6550B analyzer [18].

The measured real permeability as a function of frequency for various core sizes is shown in Fig. 3. As can be seen, the largest core with an external diameter of 152 mm exhibits the most significant change of permeability, it sharply drops to zero at a frequency of approx. 400 kHz. The real permeability characteristic for the smallest core with a diameter of 6 mm slowly descends down to 0 at 20 MHz.

TABLE I
CORE PARAMETERS FOR COMPLEX PERMEABILITY MEASUREMENTS

Core type	Dimensions OD × ID × H	Core cross section	Core volume	Core material
Unit	mm	mm ²	cm ³	-
T6	6×4×2.8	2.8	0.04	3C95
T29	29×19×10	50	3.77	3C95
T50	50×30×19.5	125	16.11	3C95
T87	87×56×20	300	66.92	3C95
T152	152×104×24	576	231.60	3C95

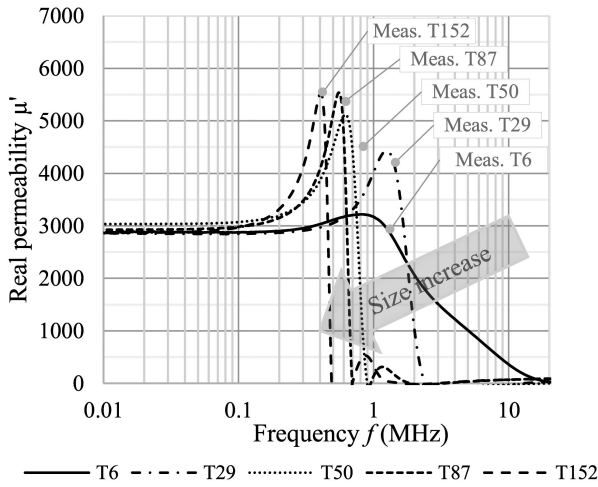


Fig. 3. 3C95 ferrite real permeability versus frequency based on experimental data.

The imaginary permeability as a function of frequency for the selected cores is shown in Fig. 4. For the largest cores, the first and most significant imaginary permeability peak is recorded and is visible for the lowest frequency at approx. 500 kHz.

B. Complex Permeability Temperature Effect

The temperature effect on the ferrites' complex permeability is shown in Figs. 5 and 6. The large ferrite samples show a high temperature dependency. At a temperature of 100 °C, the permeability peak reduces from 400 down to 250 kHz. The temperature impact on the small ferrite sample is negligible.

Plots of real and imaginary permeability for three Mn-Zn ferrite materials, 3E10, 3F36, and 3E65, are shown in Fig. 7. Characteristics were measured at 25 °C for the toroidal core T6/4/2.8 that provides the material data with the highest possible accuracy.

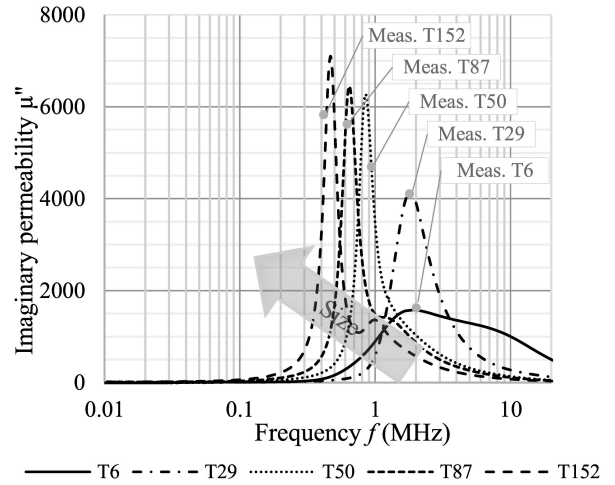


Fig. 4. 3C95 ferrite imaginary permeability versus frequency based on experimental data.

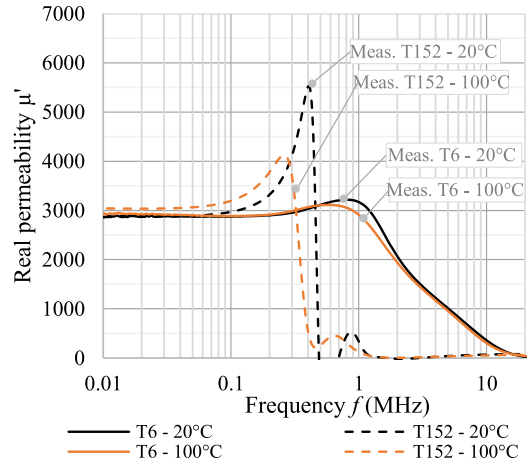


Fig. 5. 3C95 ferrite real permeability versus frequency based on experimental data.

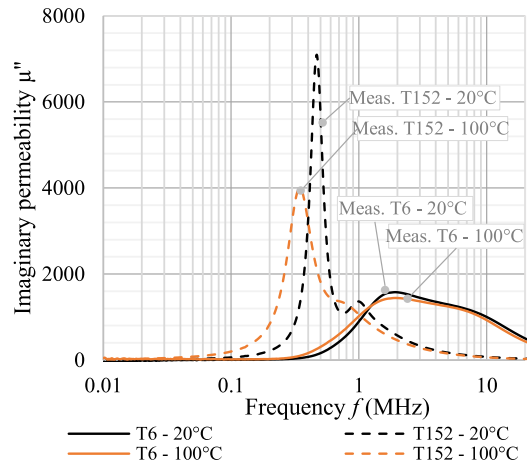


Fig. 6. 3C95 ferrite imaginary permeability versus frequency based on experimental data.

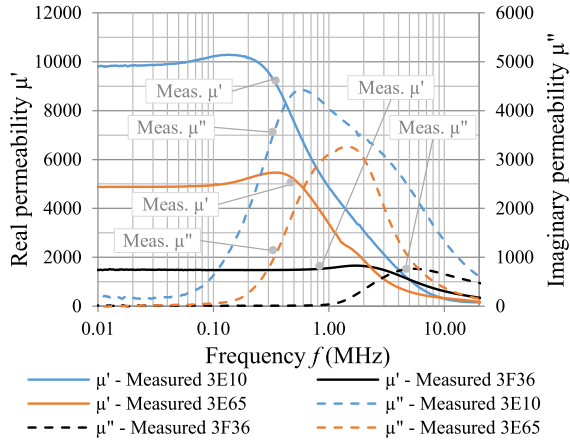


Fig. 7. Complex permeability versus frequency based on experimental data.

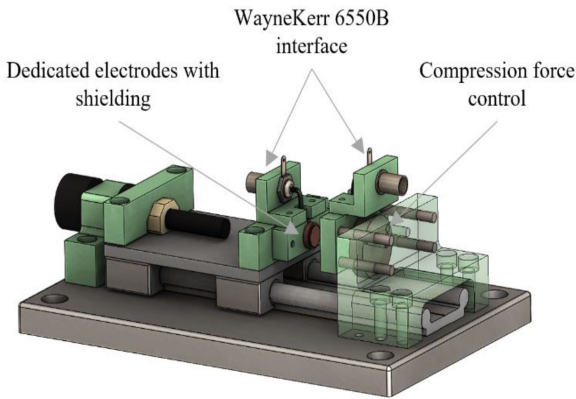


Fig. 8. Ferrite electrical properties measurement fixture.

III. COMPLEX PERMITTIVITY

In order to define the ferrite electrical characteristics for the dielectric constant ε and conductivity σ a dedicated test fixture was developed as presented in Fig. 8. The test fixture has three exchangeable sets of electrodes that can be used for measurement of custom shapes: two electrodes, with diameters of 10 and 1.8 mm, for testing rod cores, and one electrode for testing rectangular cross section cores with dimensions 2.4 by 10 mm. Each electrode is shielded to minimize fringing fields [19].

The test fixture is equipped with strain gauges to control the ferrite stress during measurements. The permittivity and conductivity characteristics are measured using a Wayne Kerr 6550B analyzer up to 20 MHz. During the test, a sample is placed between the copper electrodes, and admittance is measured. The real part of the admittance determines the frequency-dependent conductance G_P . The imaginary permittivity is calculated based on the conductance characteristic. The imaginary part of the admittance gives the core real permittivity characteristics [20], [21]. All tested samples have metallized contact surfaces to minimize contact resistance. Before metallization, the test surfaces were polished, and thin layers of graphite paint were applied on test surfaces. To minimize the impedance measurement error, open, short, and load compensations of the test fixture are

 TABLE II
CORE PARAMETERS FOR COMPLEX PERMEABILITY MEASUREMENTS

Parameter	Sample 1	Sample 2	Sample 3	Sample 4
Shape				
Dimensions	A×B 10×10 mm	A×B 10×5 mm	A×B×C 10×2.4×10 mm	A×B 1.8×18 mm
Core cross section	78.5 mm ²	78.5 mm ²	24 mm ²	2.5 mm ²
Core volume	793 mm ³	393 mm ³	58 mm ³	46 mm ³
Material	3C90	3C90	3C90	3C90
Dimensional resonance frequency	1.28 MHz	1.28 MHz	7.49 MHz	13.7 MHz
D_R	10 mm	10 mm	2.4 mm	1.8 mm

performed before each test. For the short compensation, both electrodes are shortened by closing the fixture such that both electrodes are in contact. During the open compensation, the test fixture is loaded with an 18 mm plastic dummy. During the load compensation, it is loaded with a 50 Ω resistor and 100 pF capacitor. The relationship between admittance and complex permittivity is defined as follows:

$$Y_P = G_P + j\omega C_P \quad (2)$$

$$\varepsilon_P = \varepsilon'_P - j\varepsilon''_P \quad (3)$$

$$\varepsilon'_P = \frac{C_P d}{\varepsilon_0 A_c} \quad (4)$$

$$\varepsilon''_P = \frac{G_P d}{\omega \varepsilon_0 A_c} = \frac{\sigma}{\omega \varepsilon_0} \quad (5)$$

where G_P is the measured conductance, C_P is the measured capacitance, ε_P is the parallel relative complex permittivity, ε'_P is the real component of the parallel relative complex permittivity, ε''_P is the imaginary component of the parallel relative complex permittivity, ε_0 is the vacuum permittivity,

d is the tested sample thickness, A_c is the test sample cross section, and σ is the material conductivity.

A. Complex Permittivity Physical Samples Size Effect

The sample size selection plays an important role in magnetic material testing as the dimensions of the tested sample may fall within the range of the electromagnetic wavelength for the frequencies of interest; and thus, the developed dimensional resonance may dominate the measured core parameters. In order to demonstrate the influence of sample size on the complex permittivity characteristics, four samples of the same material were tested. The sample details are listed in Table II. Samples differ from each other in their cross-sectional dimensions, which directly affect the dimensional resonance when the smallest dimension perpendicular to the applied electric or magnetic field equals one half of a wavelength.

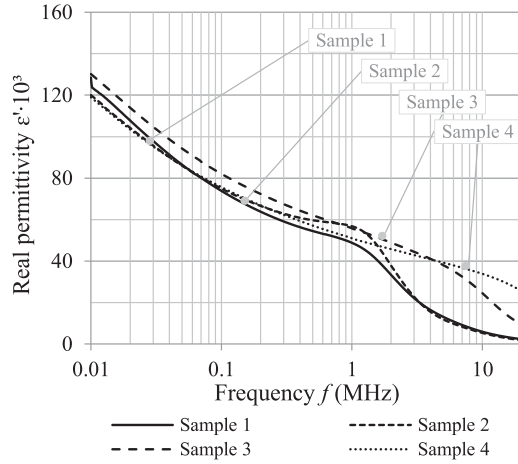


Fig. 9. 3C90 ferrite real permittivity versus frequency based on experimental data.

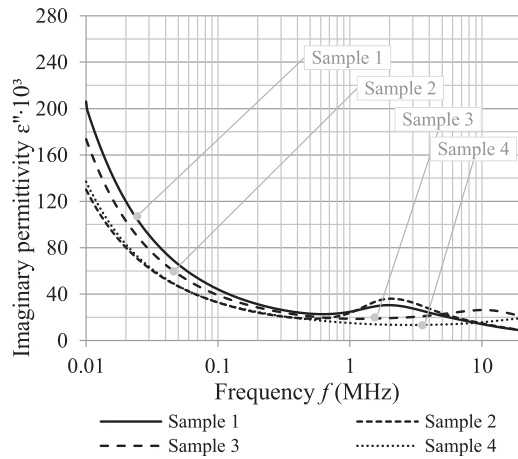


Fig. 10. 3C90 ferrite imaginary permittivity versus frequency based on experimental data.

Next, the samples listed in Table II were tested in the proposed test fixture. The electrical properties of the tested samples were extracted from the admittance. Plots of real and imaginary permittivity as a function of frequency are shown in Figs. 9 and 10, respectively. For tested Samples 1 and 2, the real permittivity drops sharply at 1.3 MHz, and for Sample 3, the real permittivity drops at 7 MHz while Sample 4 shows real permittivity decreasing gradually as frequency increases. Imaginary permittivity characteristics at the mentioned frequencies, 1.3 and 7 MHz, show significant loss increases. As illustrated in both plots, the high-frequency effects are visible in the tested samples, and the difference in the measured complex permittivity for high frequencies is the result of the dimensional resonance developed due to the sample size. The sample height (in the direction of the applied E field) has little effect on the measured complex permittivity. The difference in the measured imaginary permittivity is explained by the material parameter tolerance spread due to manufacturing and processing. Usually, ferrite properties are specified with a tolerance of $\pm 20\%$ [18], test samples were made from different material batches, and, therefore, the frequency

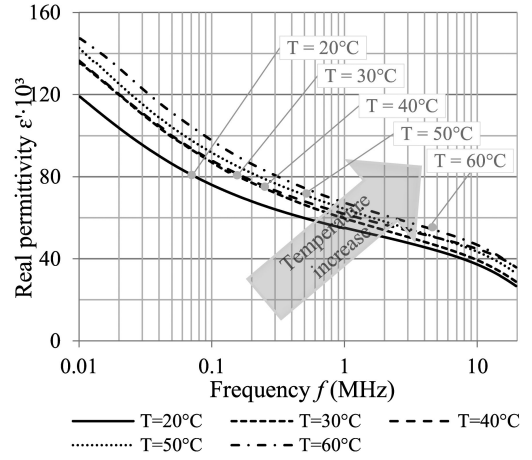


Fig. 11. 3C90 ferrite real permittivity versus frequency and temperature based on experimental data.

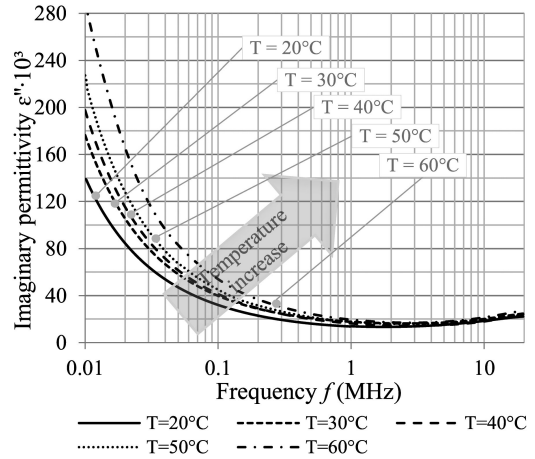


Fig. 12. 3C90 ferrite imaginary permittivity versus frequency and temperature based on experimental data.

characteristic would vary in the low-frequency region. In addition, the samples were machined from ferrite blocks. Machining impacts ferrite properties due to surface processing, and as a result, it influences the imaginary permittivity characteristic.

B. Complex Permittivity Temperature Effect

The temperature influence on ferrite dielectric properties is shown in Figs. 11 and 12. Ferrite materials show a high temperature dependency. Temperature increase typically results in an increase in the real permittivity in the analyzed frequency range. Imaginary permeability also increases with the temperature; the biggest parameter variation is observed at low frequencies.

C. Measurement Extrapolation Using Constant-Phase Elements (CPE)

The measured complex permittivity characteristics can be significantly impacted by the dimensional resonance, as can be seen in Figs. 9 and 10. However, the dimensional resonance effect can be eliminated by using an equivalent circuit to extrapolate the measurements. The equivalent circuit assumes that

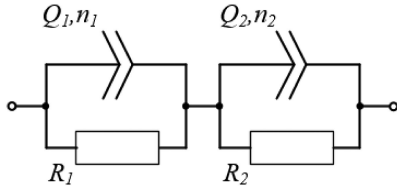


Fig. 13. Equivalent electrical circuit of a Mn-Zn ferrite based on CPE.

 TABLE III
 3C90 CPE EQUIVALENT PARAMETERS TO MODEL REAL AND IMAGINARY PERMITTIVITY

Ferroxcube 3C90			
R_1	1.00×10^6	R_2	8.70×10^5
Q_1	1.196×10^{-6}	Q_2	2.967×10^{-10}
n_1	0.173	n_2	0.928

the extracted parameters are examined at frequencies where frequency effects are not present and allow the modeling of core behavior, regardless to its size and operating frequency. Proof of the method is validated up to 5 MHz, due to sample's minimum size availability.

The proposed equivalent circuit model is based on CPE [22]. The equivalent circuit is a parallel network of resistance and CPE pairs connected in series stages that represent the ferrite granular structure. The CPE is advantageous for modeling imperfect capacitance, where the effective capacitance and resistance are decreasing as frequency increases. The CPE element is characterized by two parameters: Q and n . For $n = 1$, the CPE corresponds to a pure capacitor. The two-stage equivalent circuit of a Mn-Zn ferrite with CPE is shown in Fig. 13.

The complex impedance and its real and imaginary components are as follows:

$$Z(\omega) = \frac{R_1}{1 + (j\omega)^{n_1} Q_1 R_1} + \frac{R_2}{1 + (j\omega)^{n_2} Q_2 R_2} \quad (6)$$

$$\begin{aligned} \text{Re } Z(\omega) &= \frac{R_1 (1 + \omega^{n_1} \cos(\frac{\pi n_1}{2}) Q_1 R_1)}{1 + \omega^{n_1} Q_1 R_1 (2 \cos(\frac{\pi n_1}{2}) + \omega^{n_1} Q_1 R_1)} \\ &+ \frac{R_2 (1 + \omega^{n_2} \cos(\frac{\pi n_2}{2}) Q_2 R_2)}{1 + \omega^{n_2} Q_2 R_2 (2 \cos(\frac{\pi n_2}{2}) + \omega^{n_2} Q_2 R_2)} \end{aligned} \quad (7)$$

$$\begin{aligned} \text{Im } Z(\omega) &= - \frac{\omega^{n_1} R_1 \sin(\frac{\pi n_1}{2}) Q_1 R_1}{1 + \omega^{n_1} Q_1 R_1 (2 \cos(\frac{\pi n_1}{2}) + \omega^{n_1} Q_1 R_1)} \\ &- \frac{\omega^{n_2} R_2 \sin(\frac{\pi n_2}{2}) Q_2 R_2}{1 + \omega^{n_2} Q_2 R_2 (2 \cos(\frac{\pi n_2}{2}) + \omega^{n_2} Q_2 R_2)} \end{aligned} \quad (8)$$

The equivalent circuit parameters for 3C90 ferrite are listed in Table III.

The extrapolation accuracy depends on the last point used in the curve fitting. The selected point shall not be affected by high-frequency effects, such as eddy currents and dimensional

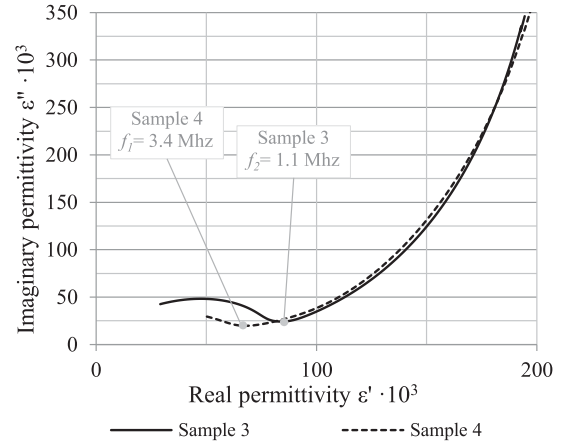


Fig. 14. Imaginary permittivity versus real permittivity based on experimental data.

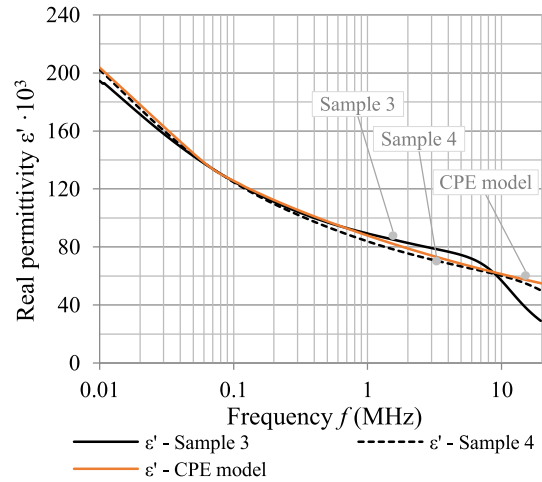


Fig. 15. 3C90 ferrite real permittivity versus frequency based on experimental data.

resonance. As a general rule, the selected point is determined by the change of function monotony in the plane of imaginary versus real permittivity. Graphical representation of the function monotony change is shown in Fig. 14. For tested Sample 3, the frequency point refers to 1.1 MHz, while for Sample 4, the frequency point refers to 3.4 MHz.

Real and imaginary permittivity frequency characteristic based on the equivalent circuit are shown in Figs. 15 and 16, respectively. The extrapolated measurement follows the material natural characteristics without core size effect.

Four Mn-Zn ferrite materials were selected to determine the electrical properties. Thus, the obtained permittivity frequency characteristic provides the material data with the highest possible accuracy for the further calculation. Plots of real and imaginary permittivity as a function of frequency are shown in Figs. 17 and 18, respectively. Widely different materials, such as 3E10, 3C95, 3E65, and 3F36, are presented with the same value of permittivity in the manufacturers' specifications. This does not represent the true situation and can generate significant error during design.

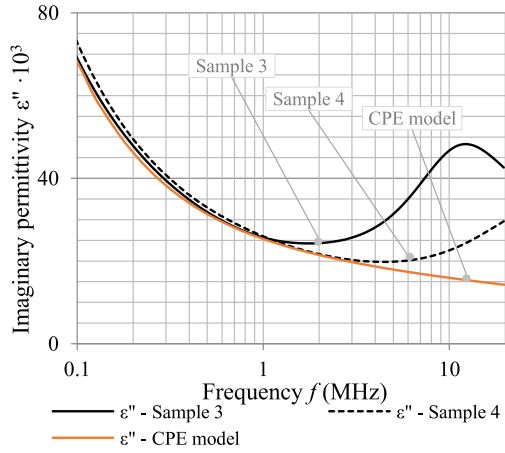


Fig. 16. 3C90 ferrite imaginary permittivity versus frequency based on experimental data.

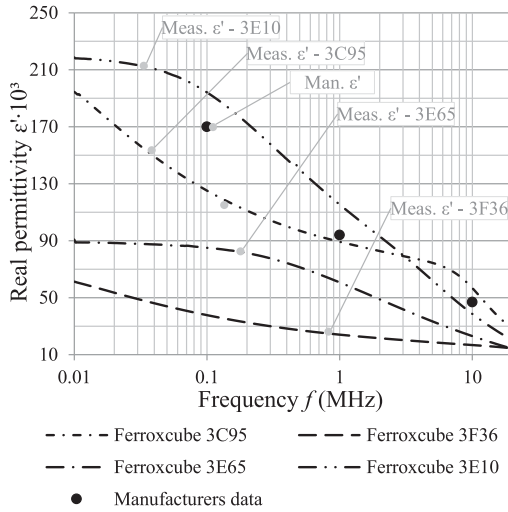


Fig. 17. Real permittivity versus frequency characteristic based on experimental data and CPE extrapolation.

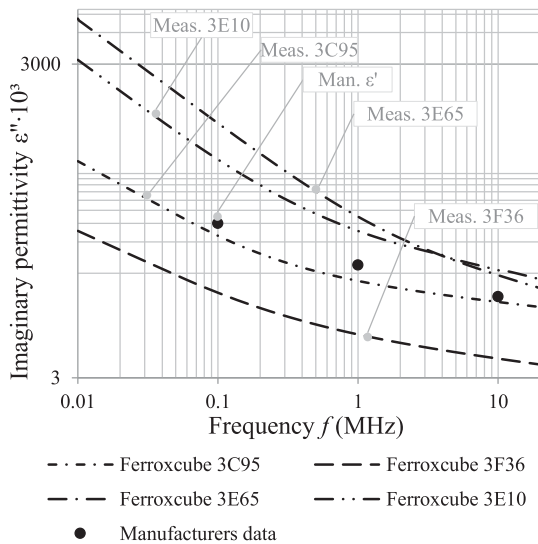


Fig. 18. Imaginary permittivity versus frequency characteristic based on experimental data and CPE extrapolation.

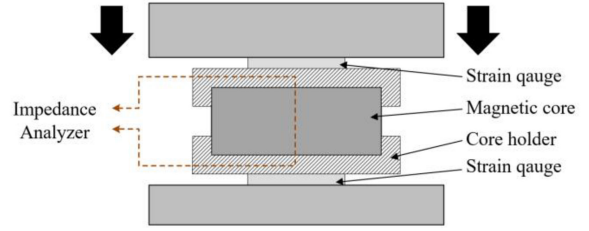


Fig. 19. Measurement setup for testing impact of mechanical stress on magnetic permeability.

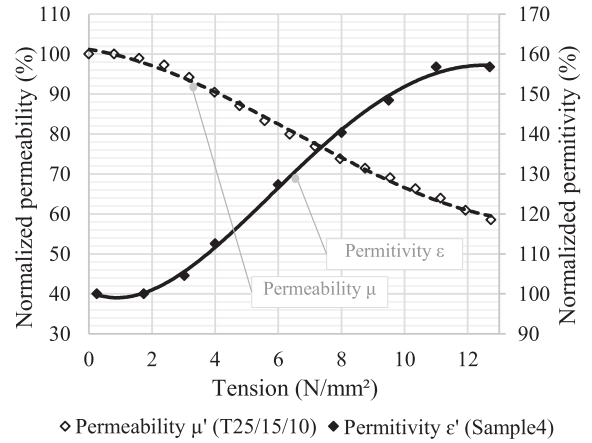


Fig. 20. 3C90 ferrite permeability and permittivity change versus mechanical pressure, based on experimental data.

IV. FORCE IMPACT ON FERRITE PERMEABILITY AND PERMITTIVITY

The proposed test fixture for the ferrite permittivity measurements is equipped with strain gauges for compression force control, therefore it was possible to measure the effect of stress on ferrite permittivity. The force applied during measurements minimizes the negative impact of sample contact resistance. However, excessive force can cause significant parameter deterioration. In practical applications, the magnetic components may be subjected to mechanical stress due to winding processes, potting, and/or thermal expansion. The grinding process may introduce internal stress to the core that affect the overall performance. In order to measure the effect of stress on ferrite permeability, an additional fixture was built as shown in Fig. 19. Permeability measurements were performed on a ring core with an external diameter of 25 mm, an inner diameter of 15 mm, and a height of 10 mm with one turn.

The mechanical stress impact on 3C90 ferrite permeability and permittivity is shown in Fig. 20. Permeability decreases with increasing pressure. Permittivity is somewhat complementary to permeability; it increases with the increase in pressure.

V. POWER LOSSES

Material selection is difficult and needs to be examined case-by-case for each design and application. Accurate core loss prediction is an essential part of magnetic component design process in power electronics applications. State-of-the-art methods are based on the sinusoidal excitation loss measurement

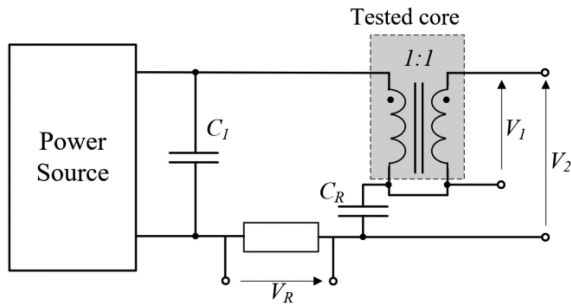


Fig. 21. Core power loss measurement setup with sinusoidal excitation.

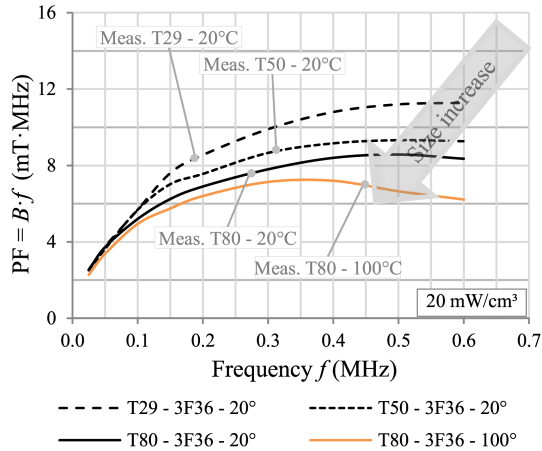


Fig. 22. Performance factor versus frequency for 3F36 material based on experimental data.

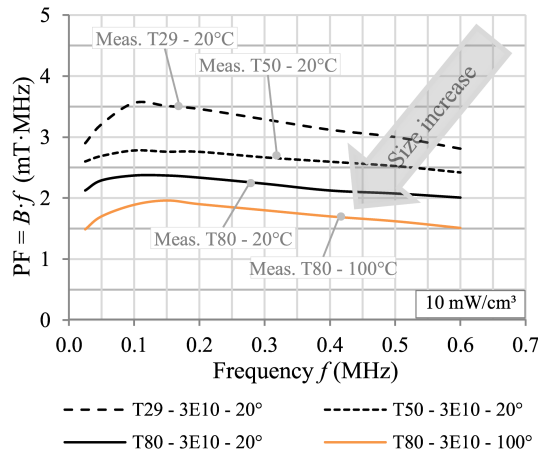


Fig. 23. Performance factor versus frequency for 3E10 material based on experimental data.

for small cores with an external diameter of 29 mm. This is a foundation for the widely used Steinmetz equation. However, the Steinmetz equation parameters are then provided as constant, regardless of core shape and size. This is counter intuitive to the findings presented in previous sections. As already shown, the dimensions of the tested Mn-Zn ferrites affect the measured complex permeability and permittivity, and, thus, power losses.

Note that power inductors operate at much higher loss densities than those discussed in this article. The design process of

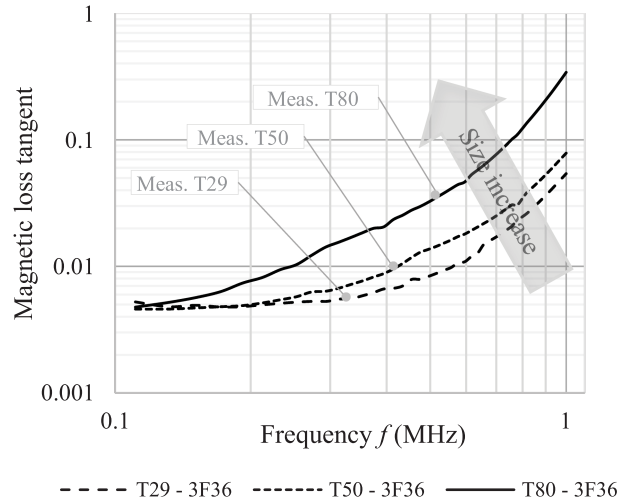


Fig. 24. Magnetic loss tangent versus frequency for 3F36 material based on experimental data.

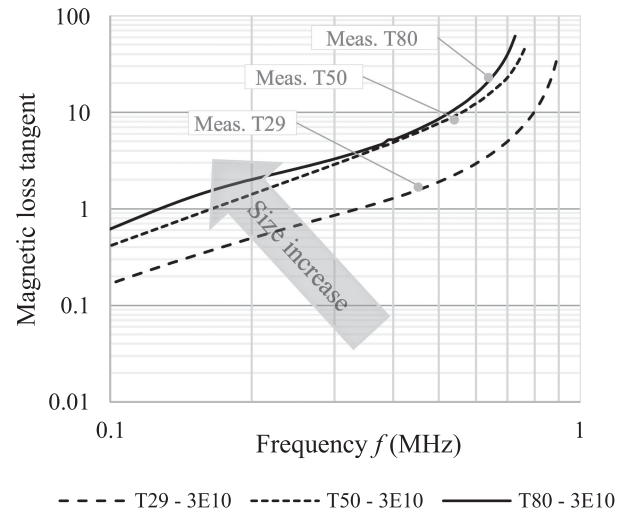



Fig. 25. Magnetic loss tangent versus frequency for 3E10 material based on experimental data.

power inductors requires different material characteristics compared with EMI filters. The crucial input data for power inductors calculations are the material characteristics measured with large signals. The ferrite complex permeability and permittivity, measured with small signals, are mainly used during the EMI filter design process. High quality material characteristics are key for a successful EMI filter design and allow the matching the filter attenuation characteristic with EMI source. EMI filters operate with small signals. Therefore, core loss comparisons are presented for relatively low loss density. But also note, some specific materials, such as 3E10, are designed for low flux density amplitudes for EMI filter applications. Measuring such materials at much higher flux densities will result in significant temperature rise, which can significantly impact the measured parameters.

A. Performance Factor

One of the most popular parameters to compare material losses as a function of the frequency is the performance factor

TABLE IV
CORE PARAMETERS FOR POWER LOSS MEASUREMENTS

Parameter	Unit	T29	T50	T80
Dimensions OD × ID × H	mm	29×19×10.5	50×30×14	80×45×17.5
Core cross section	mm ²	53	140	306
Core volume	cm ³	3.96	17.59	60.13
Core material	-	3F36/3E10	3F36/3E10	3F36/3E10
Core view	-			

[23]. The multiplication of the maximum allowed flux density B and the sinusoidal frequency f describes the performance factor PF

$$PF = B \cdot f. \quad (9)$$

A high-performance factor indicates a material that allows for operation with the highest flux density at a specific frequency and power loss density. Parameterized power loss density is an indicator that links the magnetic performance with the thermal capability of the component. Performance factor is also included in Faraday's Law and describes the effective cross-sectional area of the core

$$A_C = \frac{V_{\text{rms}} \sqrt{2}}{2\pi \cdot B \cdot f \cdot N} = \frac{V_{\text{rms}} \sqrt{2}}{2\pi \cdot PF \cdot N} \quad (10)$$

where A_C is the effective core cross section, V_{RMS} is the root-mean-square (rms) value of the voltage across the winding and N is the turns number.

The core size and operating frequency have strong impacts on the power losses. In order to show this dependency, we test samples based on a three core sizes: T29, T50, and T80 of outer diameter 29, 50, and 80 mm, respectively, made of two materials 3F36 and 3E10. Detailed cores dimensions are listed in Table IV.

The core losses were measured with the two-winding method, including an adjustable compensation capacitor to cancel the reactive voltage [24]. The measurement setup and windings arrangement are presented in Fig. 21. The test system is supplied by the amplifier AR800A3B, which is controlled by the Agilent 33220A waveform generator. Voltage and current are measured with a Tektronix MSO56 oscilloscope, equipped with a TIVH08 voltage probe and a TCP0030A current probe.

Performance factor frequency characteristics for various core sizes for 3F36 and 3E10 are shown in Figs. 22 and 23, respectively. The performance factor curves for 3F36 material show that the power loss density for the tested cores are nearly equal at low frequency, up to 100 kHz. As the frequency increases, the power losses also increase. Power losses in the larger cores increase much faster than for the small cores. At 600 kHz, the power losses for T80 core are 35% higher than for T29.

The performance factors curves for the 3E10 material show that the power loss density varies with the tested core size. Large cores have the highest losses over the entire frequency range.

The temperature influence on ferrite performance factor is shown in Figs. 22 and 23. Core losses at 100 °C were measured for the biggest core T80 in a climate chamber. Ferrite material losses show a high temperature dependency. Temperature increase resulted in a decrease of performance factor in the analyzed frequency range for both materials 3E10 and 3F36.

In all cases, the loss density increases with increased core size and the losses are significantly higher than predicted by the published material data. This increase in loss density is due to eddy currents and a dimensional resonance which may lead to nonuniform magnetic flux distribution in the core cross section.

Eddy current losses are the result of an alternating magnetic flux in the conductive material, which induce eddy currents in that material. The magnitude of this loss depends not only on the flux density and material conductivity but also on the size and shape of the ferrite core. Section III shows that the conductivity of the ferrite strongly varies with frequency and is different for different materials.

Dielectric loss in Mn-ZN is caused by relatively high permittivity. Therefore, for the ferrites, the dielectric loss becomes an important loss component at high frequency. At hundreds of kilohertz to several MHz frequency, dependent on core size, the imaginary part of the complex permittivity will exhibit a peak and the dielectric loss increases significantly, as shown in Fig. 10.

B. Loss Tangent

Loss tangent is a widely used parameter to describe the power loss, and is given by

$$\tan \delta_m = \frac{R_S}{\omega L_S} = \frac{\mu''_S}{\mu'_S} \quad (11)$$

where δ_m is the loss angle (the phase angle between B and H).

Figs. 24 and 25 show the magnetic loss tangent of the tested samples. It can be observed that the loss tangent of the larger cores is the highest for the frequency range of interest. The magnetic loss tangent follows the performance factor measurement. Measurement of loss tangent, which is based on frequency characteristics of the complex permeability at low-field amplitude, is faster and quicker than performance factor, it may be used as the primary method to assess the ferrite core performance

VI. CONCLUSION

A quality design of magnetic components for high-frequency applications requires detailed information on magnetic materials. This article develops measurements methods to determine the critical material parameters. A significant outcome from the testing is the observation that permeability, permittivity, and power loss vary with the physical core size. In general, the performance deteriorates as size increases. The performance drop in permeability and power loss is seen at lower frequency for large size cores. We also see that the permeability and permittivity change with the levels of applied compression force and temperature that can be experienced in applications. The CPE method has been introduced to enable accurate modelling of the core permittivity versus frequency.

APPENDIX I

Measured ferrite complex permeability and permittivity characteristic data for tested materials are presented in Tables V and VI shown at this previous page, respectively.

TABLE V
REAL AND IMAGINARY PERMITTIVITY CHARACTERISTIC

Frequency (MHz)	Ferroxcube 3E10		Ferroxcube 3F36	
	ϵ'	ϵ''	ϵ'	ϵ''
0.01	218962	3292135	61262	76243
0.1	85011	814288	36788	18587
0.2	81232	413498	32208	13651
0.3	77352	289593	29893	11600
0.4	74238	220139	28382	10426
0.5	71206	180479	27275	9645
0.6	68758	156171	26410	9080
0.7	66158	135719	25703	8646
0.8	64065	122039	25109	8299
0.9	62211	111676	24598	8013
1.0	60678	103988	24151	7773
2.5	44943	56722	20622	6134
5.0	33149	39108	18321	5250
7.5	27023	32489	17081	4842
10.0	22925	28670	16284	4576
12.5	19845	26035	15679	4384
15.0	17632	24247	15202	4236
17.5	15747	22909	15810	4116
20.0	14282	21537	14484	4018
Frequency (MHz)	Ferroxcube 3E65		Ferroxcube 3C95	
	ϵ'	ϵ''	ϵ'	ϵ''
0.01	90788	8162193	213662	373678
0.1	85011	829638	123674	64461
0.2	81232	413498	111522	45085
0.3	77555	284607	105046	37712
0.4	74238	220139	100663	33702
0.5	71206	180479	97373	31130
0.6	68758	156171	94753	29312
0.7	66158	135719	92583	27943
0.8	64364	123885	90738	26867
0.9	62211	111676	89135	25991
1.0	60678	103988	87722	25261
2.5	44934	56722	76209	20441
5.0	33149	39108	68389	17928
7.5	27023	32489	64083	16694
10.0	22925	28670	61228	15931
12.5	20097	26247	59147	15362
15.0	17632	24237	57448	14918
17.5	15747	22909	56021	14556
20.0	14201	21253	54880	14257

TABLE VI
REAL AND IMAGINARY PERMEABILITY CHARACTERISTIC

Frequency (MHz)	Ferroxcube 3E10		Ferroxcube 3F36	
	μ'	μ''	μ'	μ''
0.01	9812	228	1482	8
0.1	10215	621	1479	11.2
0.2	10150	2020	1478	9.8
0.3	9542	3230	1480	10.3
0.4	8529	4032	1483	10.5
0.5	7475	4375	1488	13.1
0.6	6659	4418	1499	13.7
0.7	6024	4349	1509	16.7
0.8	5549	4251	1522	20.4
0.9	5207	4156	1537	25.6
1.0	4806	4025	1561	38.2
2.5	2532	3264	1561	503
5.0	1060	2400	1078	763
7.5	524	1776	785	728
10.0	297	1315	606	650
12.5	222	1052	513	593
15.0	173	831	445	545
17.5	161	716	392	508
20.0	155	596	342	471
Frequency (MHz)	Ferroxcube 3E65		Ferroxcube 3C95	
	μ'	μ''	μ'	μ''
0.01	5100	10.7	3085	2.3
0.1	5156	57.8	3095	4.5
0.2	5253	290	3124	15.1
0.3	5444	789	3181	32.6
0.4	5425	1339	3265	79.8
0.5	5166	1994	3355	179
0.6	4797	2420	3418	314
0.7	4392	2712	3452	469
0.8	4022	2897	3464	626
0.9	3638	3036	3449	816
1.0	3320	3121	3403	996
2.5	264	2449	1855	1630
5.0	153	932	1078	1388
7.5	141	546	677	1249
10.0	131	371	375	1069
12.5	127	270	215	911
15.0	120	213	102	742
17.5	115	180	57.3	620
20.0	109	147	24.5	528

ACKNOWLEDGMENT

The authors would like to thank Edward Herbert for his valuable and constructive suggestions during the planning and development of this work. This article is an extension of work presented in PSMA reports [13], [14]. A companion article on the analysis and experimental investigation of flux distribution has also been submitted to *IEEE TPEL* [24].

REFERENCES

- [1] E. Hoene, G. Deboy, C. R. Sullivan, and G. Hurley, "Outlook on developments in power devices and integration: Recent investigations and future requirements," *IEEE Power Electron. Mag.*, vol. 5, no. 1, pp. 28–36, Mar. 2018.
- [2] G. Hurley, T. Merkin, and M. Duffy, "The performance factor for magnetic materials revisited: The effect of core losses on the selection of core size in transformers," *IEEE Power Electron. Mag.*, vol. 5, no. 3, pp. 26–34, Sep. 2018.
- [3] M. S. Rylko, B. J. Lyons, J. G. Hayes, and M. G. Egan, "Revised magnetics performance factor and experimental comparison of high-flux materials for high-current DC-DC inductors," *IEEE Trans. Power Electron.*, vol. 26, no. 8, pp. 2112–2126, Aug. 2011.
- [4] J. Biela, M. Schweizer, S. Waffler, and J. W. Kolar, "SiC vs. Si evaluation of potentials for performance improvement of power electronics converter system by SiC power semiconductors," *IEEE Trans. Ind. Electron.*, vol. 58, no. 7, pp. 2872–2882, Jul. 2011.
- [5] G. R. Skutt, "High-frequency dimensional effects in Ferrite-core magnetic devices," Ph.D. dissertation, Virginia Polytech. Inst., Blacksburg, VA, USA, 1996.

- [6] G. R. Skutt and F. C. Lee, "Characterization of dimensional effects in ferrite-core magnetic devices," in *Proc. PESC Rec. 27th Annu. IEEE Power Electron. Specialists Conf.*, 1996, pp. 1435–1440.
- [7] P. Pengfei and Z. Ning, "Magnetodielectric effect of Mn-Zn ferrite at resonant frequency," *J. Magnetism Magn. Mater.*, vol. 416, pp. 256–260, Oct. 2016.
- [8] B. D. Cullity and C. D. Graham, *Introduction to Magnetic Materials*, New York, NY, USA: Wiley, 2009.
- [9] R. F. Soohoo, *Theory and Application of Ferrites*, Englewood Cliffs, N.J., USA, Prentice-Hall, 1960.
- [10] F. G. Brockman, P. H. Dowling, and W. G. Steneck, "Dimensional effects resulting from a high dielectric constant found in a ferromagnetic ferrite," *Phys. Rev.*, vol. 77, Jan. 1950, Art. no. 1.
- [11] M. Kaćki, M. S. Rylko, J. G. Hayes, and C. R. Sullivan, "Magnetic material selection for EMI filter," in *Proc. IEEE Energy Convers. Congr. Expo.*, 2017, pp. 2350–2356.
- [12] M. Kaćki, M. S. Rylko, J. G. Hayes, and C. R. Sullivan, "A practical method to define high frequency electrical properties of MnZn ferrites," in *Proc. IEEE Appl. Power Electron. Conf. Expo.*, 2020, pp. 216–222.
- [13] M. Kaćki, M. S. Rylko, and E. Herbert, "PSMA-SMA special project – Phase I, investigation on magnetic flux propagation in ferrite cores," Power Source Manuf. Assoc., 2018. [Online]. Available: <https://www.pdma.com/sites/default/files/uploads/files/Magnetic%20Core%20Dimensional%20Effects%20Kacki%20SMA%20Magnetics%20S.pdf>
- [14] M. Kaćki, M. S. Rylko, and E. Herbert, "PSMA-SMA special project – Phase II, investigation on magnetic flux propagation in ferrite cores," Power Source Manuf. Assoc., 2020. [Online]. Available: <https://www.pdma.com/sites/default/files/uploads/files/Preliminary%20Report%20Phase%20II%20190310%20S.pdf>
- [15] Accessed: Feb. 7, 2022. [Online]. Available: www.ferroxcube.com
- [16] J. Xu, M. Y. Koledintseva, Y. Zhang, Y. He, B. Matlin, and R. E. DuBroff, "Complex permittivity and permeability measurements and finite-difference time-domain simulation of ferrite materials," *IEEE Trans. Electromagn. Compat.*, vol. 52, no. 4, pp. 878–887, Nov. 2010.
- [17] V. Radonic, N. Blaz, and L. J. Živanov, "Measurements of complex permeability using short coaxial lone reflection method," *Acta Physica Polonica Ser. A*, vol. 117, no. 5, pp. 820–824, 2010.
- [18] Accessed: Jan. 10, 2022. [Online]. Available: www.waynecerttest.com
- [19] M. Kaćki, M. S. Rylko, J. G. Hayes, C. R. Sullivan, and E. Herbert, "Magnetic core dimensional effects - flux propagation in ferrites," in *Proc. PSMA Workshop IEEE Appl. Power Electron. Conf.*, 2018, pp. 1–37.
- [20] E. C. Snelling, *Soft Ferrites: Properties and Applications*. Oxford, U.K.: Newnes-Butterworth, 1969.
- [21] W. H. Hayat, Jr., *Engineering Electromagnetics*. New York, NY, USA: McGraw-Hill, 1981.
- [22] Accessed: Jan. 18, 2022. [Online]. Available: www.abc.chemistry.bsu.edu/vi/analyser
- [23] T. Kauder and K. Hameyer, "Performance factor comparison of nanocrystalline, amorphous, and crystalline soft magnetic materials for medium-frequency applications," *IEEE Trans. Magn.*, vol. 53, no. 11, Nov. 2017, Art no. 8401504.
- [24] M. Mu, "High frequency magnetic core loss study," Ph.D. dissertation, Virginia Polytech. Inst., Blacksburg, VA, USA, 2013.



Marcin Kaćki received the M.Eng.Sc. degree in electrical engineering from the AGH University of Science and Technology, Kraków, Poland, in 2012. He is currently working toward the Ph.D. degree in high frequency magnetics with the University College Cork, Cork, Ireland.

In 2011, he joined the R&D team with SMA Magnetics, Modniczka, Poland, where he is currently a Senior Engineer. His research interests include optimization and integration of the magnetic components with emphasis on EMC filters, numerical analysis,

and power electronics.



Marek S. Rylko (Member, IEEE) received the B.E. degree in electrical engineering from the University of Bielsko-Biala, Bielsko, Poland, in 2003, the M.Eng.Sc. degree in electrical engineering from the Silesian University of Technology, Gliwice, Poland, in 2004, and the Ph.D. degree in electrical engineering from University College Cork, Cork, Ireland, in 2011.

From 2005 to 2010, he was working on the Ph.D. with Power Electronics Research Laboratory, where he was involved in various industrial activities. Following this, he joined the Research Staff of DTW SP. Z.O.O., Zabierzow, Poland, that was subsequently rebranded to SMA Magnetics SP. Z.O.O. and he is currently heading R&D activities. His research interests include dc–dc and dc–ac converter topologies, power electronics, with emphasis on analysis, optimization, and integration of the magnetic components in power electronic converters for automotive and energy applications.



John G. Hayes (Senior Member, IEEE) received the B.E. degree from the University College Cork (UCC), Cork, Ireland, the M.S.E.E. degree from the University of Minnesota, Minneapolis, St. Paul, MN, USA, the M.B.A. degree from California Lutheran University, Thousand Oaks, CA, USA, and the Ph.D. degree from UCC, in 1986, 1989, 1993, and 1998, respectively.

From 1986 to 1988, he was a Research Fellow of power electronics under Prof. N. Mohan with the University of Minnesota. From 1988 to 1990, he was with

the Power One, Inc., Camarillo, CA, USA, designing linear and switching ac/dc power converters. In 1990, he joined the General Motors Advanced Technology Vehicle (formerly Hughes Aircraft Company and Delco Electronics), Culver City, CA, USA and later Torrance, CA, USA, where he was a Design Engineer and a Technical Manager in the fields of propulsion drives and battery charging for electric vehicles, especially for heavy-duty vehicles and the General Motors EV1 electric car. From 1995 to 1997, he was a Howard Hughes Corporate Fellow (Ph.D. part-time) while continuing to work as a Design Engineer with General Motors, Detroit, MI, USA. Subsequently, he was a Technical Manager on EV battery chargers and infrastructure. He joined the academic staff with UCC in late 2000 and currently teaches power engineering and power electronics and drives. He directs the Power Electronics Research Laboratory, UCC. He is the lead author with coauthor Dr. A. Goodarzi, his former GM colleague and the CEO of Magmotor, Worcester, MA, USA on *Electric Powertrain: Systems, Power Electronics and Drives for Electric, Hybrid and Fuel Cell Vehicles* (English-language edition, Wiley, 2018; Chinese-language edition, China Machine Press, 2021). His research interests include power electronics, machines, and magnetics for automotive, and energy applications.



Charles R. Sullivan (Fellow, IEEE) received the B.S. degree (with highest Hons.) in electrical engineering from Princeton University, Princeton, NJ, USA, in 1987, and the Ph.D. degree in electrical engineering from the University of California, Berkeley, CA, USA, in 1996.

He was with Lutron Electronics, Coopersburg, PA, USA, designing electronic ballasts. He is currently a Professor with the Thayer School of Engineering at Dartmouth, Hanover, NH, USA, where he is also the Director of the Power Management Integration

Center. He is the holder of 43 U.S. patents. His research interests include modeling and design optimization of magnetics and other passive components for high-frequency power conversion and wireless power transfer.

Dr. Sullivan was the recipient of the Power Electronics Society Modeling and Control Technical Achievement Award, in 2018 and three Power Electronic Society Prize Paper Awards. He is the Co-Founder of Resonant Link, Inc., South Burlington, VT, USA.